PNAS RESEARCH ARTICLE | ENGINEERING

Modular multi-degree-of-freedom soft origami robots with reprogrammable electrothermal actuation

Shuang Wu[a,1], Tuo Zhao[b,1], Yong Zhu[a,2], and Glaucio H. Paulino[b,c,2]

Edited by Yonggang Huang, Northwestern University, Glencoe, IL; received December 22, 2023; accepted March 12, 2024

Soft robots often draw inspiration from nature to navigate different environments. Although the inching motion and crawling motion of caterpillars have been widely studied in the design of soft robots, the steering motion with local bending control remains challenging. To address this challenge, we explore modular origami units which constitute building blocks for mimicking the segmented caterpillar body. Based on this concept, we report a modular soft Kresling origami crawling robot enabled by electrothermal actuation. A compact and lightweight Kresling structure is designed, fabricated, and characterized with integrated thermal bimorph actuators consisting of liquid crystal elastomer and polyimide layers. With the modular design and reprogrammable actuation, a multiunit caterpillar-inspired soft robot composed of both active units and passive units is developed for bidirectional locomotion and steering locomotion with precise curvature control. We demonstrate the modular design of the Kresling origami robot with an active robotic module picking up cargo and assembling with another robotic module to achieve a steering function. The concept of modular soft robots can provide insight into future soft robots that can grow, repair, and enhance functionality.

origami | soft robot | electrothermal actuation | Kresling pattern

Significance

A plug-and-play soft modular origami robot is introduced, enabled by electrothermal actuation with highly bendable heaters. The heater, based on a stretchable silver nanowire conductor, exhibits large, reversible local bending along the crease line of the origami. Our modular origami robot draws inspiration from the segmented caterpillar body. By mimicking the rich kinematics of caterpillar segments, each robot module features reprogrammable actuation modes, i.e., extension/contraction and bending. The desired deformation modes of the modular units, bidirectional and/or steering, can be achieved on the fly. This work reports an effective actuation method that can be generally applied to origami structures (with creases) for soft robotics.

Soft robotics is a rapidly emerging field of robotics that deviates from traditional rigid-bodied robotics. Unlike their rigid counterparts, soft robots are made from flexible materials such as elastomers, gels, or fabrics, which enables them to bend, deform, and interact with the environment in ways similar to biological organisms (1–5). By imitating the pliability and adaptability of soft tissues in biological systems, soft robots display unique features. For instance, they can conform to irregular shapes, squeeze through tight spaces, and interact safely and gently with humans and delicate objects. They are also resilient to external impacts and capable of handling uncertain and dynamic environments. Soft robots provide a wide range of motions, such as crawling, slithering, swimming, and even flying (6). This versatility makes them well suited for various applications, from search and rescue operations to exploration in harsh or confined environments (7).

Extensive research has focused on locomotive soft robots; however, persistent challenges remain, such as achieving bidirectional and steering locomotion. To achieve bidirectional locomotion, researchers have drawn inspiration from nature, particularly from living organisms like caterpillars (8–11). The locomotion mechanisms of most species of caterpillars can be divided into two types—inching and crawling (12). Inspired by the inching mechanism, recently, a bidirectional soft robot was developed using distributed, programmable electrothermal actuation (8). Inspired by the crawling mechanism, a soft robot based on light-sensitive elastomer showed bidirectional locomotion under a scanning laser beam (11). However, these reported caterpillar-like robots cannot achieve steering motion due to the difficulty in disrupting the symmetrical distribution of propulsive forces that propel them forward/backward.

Steering locomotion presents an even greater challenge for soft robots. The steering mechanism for soft robotics can be classified into two types: rigid-body steering and continuous steering. A soft origami crawler has been reported with the rigid-body steering under altering magnetic field (13). A multilegged soft robot with embedded magnetic particles has shown rigid-body steering with programmed magnetization (14). Rigid-body steering allows for sharp turns but is challenging for confined spaces where on-spot rotation could be obstructed. Besides that, such soft robots enabled by magnetic field have limitations like complex control systems and confined workspace. Compared with the rigid-body steering, the continuous steering allows for natural bending during locomotion. For instance, a polymer bilayer–based soft robot was reported with steering function by controlling the local bending and anchoring (15). A combination of bidirectional locomotion and steering locomotion with local bending control can greatly enhance soft robots mobility and adaptability to their environment.

Author contributions: S.W., T.Z., Y.Z., and G.H.P. designed research; S.W. and T.Z. performed research; S.W. and T.Z. contributed new reagents/analytic tools; S.W., T.Z., Y.Z., and G.H.P. analyzed data; and S.W., T.Z., Y.Z., and G.H.P. wrote the paper.

The authors declare no competing interest.

This article is a PNAS Direct Submission.

[1]S.W. and T.Z. contributed equally to this work.

[2]To whom correspondence may be addressed. Email: yzhu7@ncsu.edu or gpaulino@princeton.edu.

This article contains supporting information online at https://www.pnas.org/lookup/suppl/doi:10.1073/pnas.2322625121/-/DCSupplemental.

Published May 6, 2024.

Modular origami-based designs (16), known for being able to program the local deformation mode in each modular unit, represent an intriguing potential solution to fulfill the local segment control of a soft robot. Kim et al. presented a foldable robotic arm taking advantage of multiple rigid origami modules assembled on demand (17). However, to mimic the multi-degree-of-freedom feature of the soft-bodied caterpillar, nonrigid origami structures are preferable, as they can harness local nonlinear deformation for multistate actuation. The intrinsic geometrical nonlinearity of these structures, such as panel stretching and bending, enables navigation of the energy landscape to achieve multi-degree-of-freedom deformation. One representative example of a nonrigid structure is the Kresling origami (18), which displays a natural coupling involving contraction, bending, and twist, enabling multiple modes of actuation. Recent studies have utilized the Kresling origami units to design robotic arms for multidirectional bending (19–21). A modular Kresling origami consisting of flexible segments, which can potentially mimic the local bending of caterpillars (in addition to bidirectional locomotion) has not been reported yet.

Different actuation methods have been studied for soft robots using a variety of stimuli, including pressure (1, 22, 23), heat (24–28), electrical field (29–31), magnetic field (32–34), and chemical potential (35, 36). Bimorph thermal actuators (24, 37, 38), which are based on a mismatch in the coefficient of thermal expansion (CTE) of two materials, have drawn much attention due to programmable operation (39), lightweight, low actuation voltage, and potential for untethered operation (e.g., via wireless charging) (40, 41). While electrothermal actuation has been employed for modest, continuous bending (8, 38, 42), their application for sharp, localized folding (e.g., for origami structure) has not been reported for soft robotics.

Here, we present a nonrigid cylindrical Kresling origami robot mimicking the multi-degree-of-freedom behavior of a *Lepidoptera* larva (caterpillar). The robot consists of multiple Kresling units, each being either active or passive. An active unit includes two electrothermal bimorph actuators, which are effectively integrated as part of the origami panels to maintain structural integrity. The active unit can deform in two modes—axial deformation and bending—by controlling the current inputs to the two actuators. In a soft robot consisting of multiple Kresling units, each active unit can be programmed individually to control the desired deformation. For instance, during the robotic steering motion, one active unit bends, serving as the steering unit; while the other active units contract axially, serving as the driving units. On the other hand, the passive units amplify the bending curvature to increase the steering efficiency of the robot further. Besides assisting on locomotion, those passive units can serve other functions such as cargo transport. A modular concept is further demonstrated to showcase potential applications of the robot.

Results

Design and Fabrication of the Caterpillar-Inspired Soft Robot. *Papilio zelicaon* is a common inhabitant of North America, consisting of 12 body segments with 3 pairs of thoracic legs and 4 pairs of prolegs (Fig. 1*A*). The 7 body segments marked in Fig. 1*B* show deformation modes of contraction and bending.

To mimic the deformation modes observed from the caterpillar segments, we designed a symmetric octagon Kresling unit consisting of two thermal bimorph actuators assembled on the two opposing sides of the unit (Fig. 1*C*). The octagon geometry is preferable as it requires less energy to deploy compared to the hexagon and square designs (*SI Appendix*, Fig. S1). The geometry of the Kresling origami is determined by four independent parameters, i.e., height H_0 in the folded state of the unit, height H_1 in the deployed (initial) state, number n of polygon edges, and the corresponding edge length b (see detailed geometrical representation of the Kresling origami in *SI Appendix*, section 1). The four geometry parameters, H_1, H_0, n, and b, need to satisfy the following design constraint to avoid the locking stage where valley folds intersect in the folded state, i.e.,

$$\left|\left(H_1/b\right)^2-\left(H_0/b\right)^2\right|\le\cot^2(\pi/n). \quad [1]$$

Fig. 1*D* shows the simulation of Kresling units connected in series mimicking the configuration of the caterpillar in Fig. 1*B*. The corresponding electric currents through all 14 actuators in the 7 units are shown in Fig. 1*E* (dimensions of the Kresling unit and the heating pattern are provided in *SI Appendix*, Fig. S2). For example, when both actuators of unit [1] ([1]-1 located on the outer side of the curved body unit and [1]-2 on the inner side) are powered with the same current, unit [1] shows a symmetric contraction just like the axial contraction of segment 1 in Fig. 1*B*. When the current inputs are applied differently on some units, e.g., unit [5], the actuator [5]-2 generates a larger deformation than the actuator [5]-1 resulting in bending deformation toward the actuator [5]-2. The bending angle θ is defined by the relative angle between the two octagon panels. Fig. 1*F* shows the bending angle θ of each Kresling unit extracted from Fig. 1*D*. It can be observed that with the increase of current input on both actuators, the contraction of the Kresling unit increases. With the increase of current difference ΔI on the two actuators, the bending angle increases. With the individual control of distributed actuators, the Kresling unit–enabled soft robot allows spatial and temporal programming of its deformation. Moreover, Fig. 1*G* (*Top*) shows that the strain energy stored in the origami unit for the bending deformation increases as the bending angle increases. In addition, the two energy minimums (Fig. 1 *G*, *Middle*) verify that the intrinsic Kresling origami design has two kinematic stable configurations. In practice, as the thermal bimorph actuators are fully integrated into the origami panels, the folding stiffness (k_r) increases; thus, the Kresling unit behaves monostably (43). This is verified by the numerical result in Fig. 1*G* (*Bottom*) showing that the strain energy monotonically increases with vertical displacement. A parametric study (*SI Appendix*, section 2) shows how the stiffness (k_r) influences the monostable and bistable behaviors, respectively.

To achieve precise actuation of the Kresling units, we designed and fabricated parallelogram-shaped thermal bimorph actuators, following the same shape as the side panel of the Kresling pattern, which can be directly integrated onto the Kresling pattern (Fig. 2). Silver nanowires (AgNWs) have been adopted as the heating material in the soft actuator due to their excellent electric conductivity and mechanical compliance (24, 44–47). In this work, we used AgNWs embedded just below the surface of a polyimide (PI) matrix (48, 49) (Fig. 2 *A*–*D*). The AgNWs (~30 μm in length and 100 nm in diameter) were in the form of a percolation network while the PI resin was spun-coated on top of the AgNW network and cured; the serpentine-shaped heating pattern was defined by laser cutting of the AgNW/PI composite film on a sacrificial substrate. The thermal actuator is a bimorph structure with a layer of commercial PI film (with an adhesive coating) and a layer of liquid crystal elastomer (LCE) ribbon laminated on the two sides of the AgNW/PI heater (Fig. 2*E*). The LCE ribbon was fabricated by mechanical stretching of a rectangular flat LCE strip synthesized by two-stage polymerization (50, 51). Plasma treatment and mechanical pressure were applied to form a strong bond between

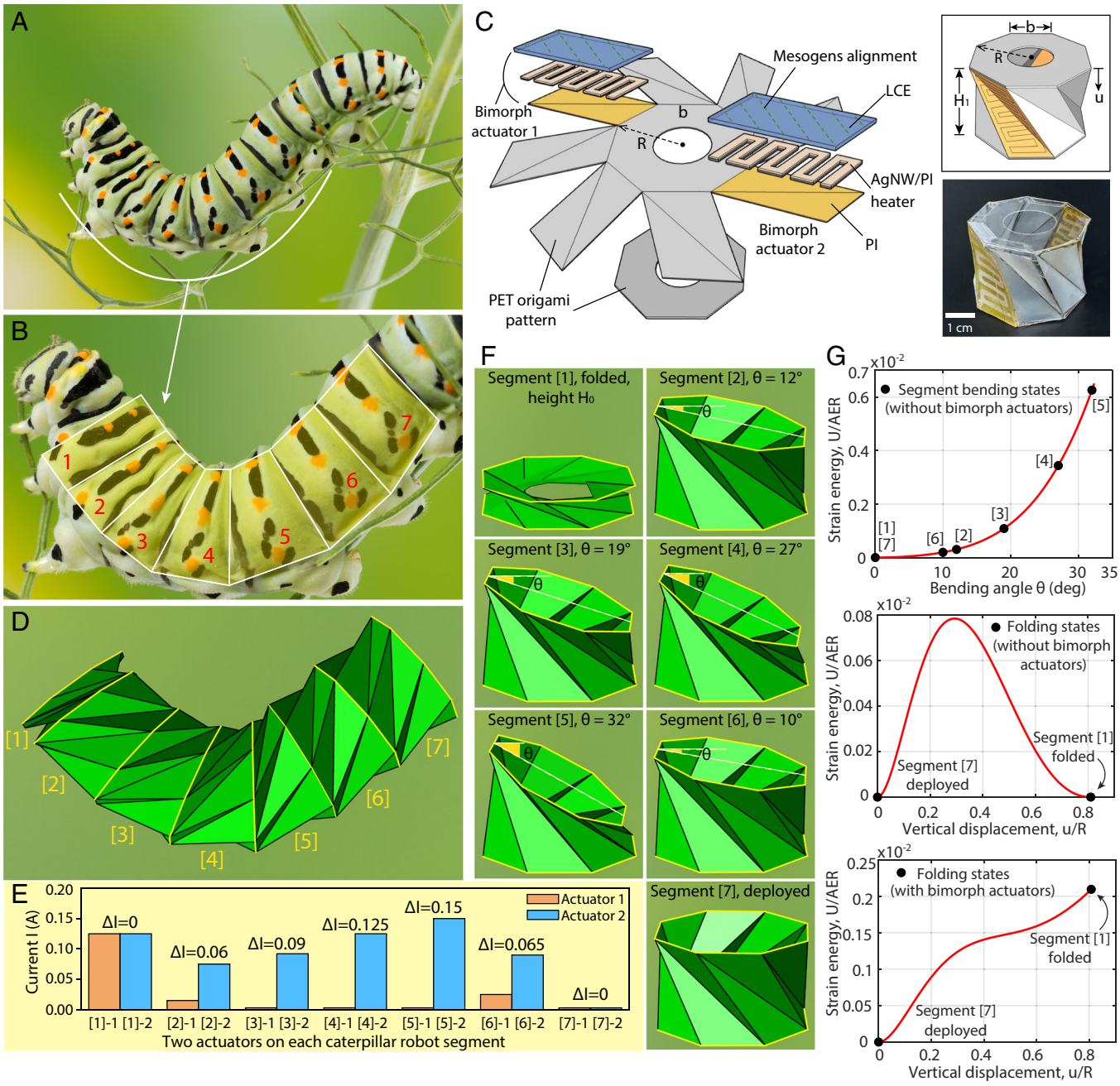

Fig. 1. Lepidoptera larva-inspired Kresling soft robot with thermal bimorph actuators. (*A*) Photograph of a late fifth instar *P. zelicaon* larva (caterpillar) in a curved configuration with local bending. (*B*) Body segments of the caterpillar marked from 1 to 7 showing different levels of local contraction and bending. (*C*) Exploded view of the robot segment composed of electrothermal bimorph actuators integrated with the origami pattern. *Insets* show the Kresling pattern (*Top*) and the physical realization (*Bottom*). Here, LCE denotes liquid crystal elastomer, AgNWs are silver nanowires, PI is polyimide, and PET is polyethylene terephthalate (thermoplastic polymer resin). The symbols H_1, b, and R denote the height of the deployed Kresling unit, the edge length, and the circumradius of the top octagon plane, respectively. (*D*) Simulated origami robot including multiple coactive Kresling units mimicking the deformed configuration of the caterpillar. (*E*) Current applied to the two actuators on each Kresling unit to induce the deformed configuration in (*D*). (*F*) Deformed Kresling units with various configurations corresponding to the robot segments. The symbols H_0, and θ denote the height of the folded Kresling unit and the bending angle between the top and bottom octagon planes, respectively. (*G*) *Top*—The stored strain energy of the Kresling origami unit without bimorph actuators of (*C*) versus bending angle; *Middle*—strain energy of the origami design without bimorph actuators of (*C*) versus vertical displacement of any vertices on the top octagon plane; *Bottom*—strain energy stored in the unit with integrated bimorph actuators of (*C*) versus vertical displacement. The strain energy (U/AER), and displacements (u/R) are normalized in the numerical simulation based on the bar-and-hinge method. Here, *A* and *E* denote the cross-sectional area and Young's modulus of the bar element, respectively. Those numeric labels (within brackets) refer to the seven configurations of the robot segments in (*F*).

the AgNW/PI composite film and the LCE ribbon. The mesogen alignment of the LCE ribbon, laid perpendicular to the longer diagonal of the parallelogram, ensures that the bending deformation of the actuators can be converted to the folding of the Kresling origami. The Kresling origami pattern was made of a piece of laser-cut polyethylene terephthalate (PET) sheet (Fig. 2*E*). Two opposing panels of the PET Kresling pattern were replaced with the thermal bimorph actuators (*SI Appendix*, Fig. S2*A*). The new pattern with integrated actuators was assembled with another octagon end panel to form a 3D Kresling unit (Fig. 2*F*). To minimize the interference to the locomotion, we have designed a hollow cylindrical region in each Kresling unit so that the wires attached to all units are inside the hollow structure of the origami, coming out from the rear end of the robot. In this way, the wires

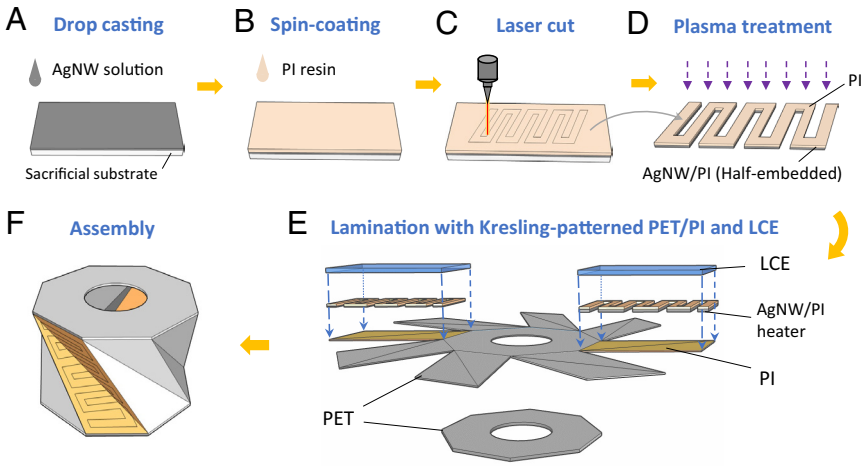

Fig. 2. Fabrication process of the Kresling unit with thermal bimorph actuators. (*A*) Drop casting of AgNWs on top of a sacrificial substrate. (*B*) Spin-coating of PI resin on top of the AgNW network. (*C*) Laser cutting the cured AgNW/PI composite film. (*D*) Peeling off the serpentine patterned AgNW/PI heater for plasma treatment. (*E*) Laminating the LCE film and patterned PET/PI sheet with the AgNW/PI heater sandwiched in between. (*F*) Assembly of the Kresling unit with integrated actuators.

do not interfere with the contact between the robot and the substrate. This simple actuator-integration approach introduces very little weight to the original origami design, leading to a compact and lightweight robotic system.

Characterization of Thermal Actuators and the Kresling Soft Robot. When electric current is applied to the AgNW network, heat is generated as a result of Joule heating and transferred to the PI layer and the LCE layer (Fig. 3*A*). An infrared (IR) image shows a uniform temperature increase along the serpentine pattern (with a line width of 1.3 mm). The sheet resistance of the AgNW/PI composite after annealing was 0.55 Ω/sq, resulting in a total resistance of 40.7 Ω for each actuator. The dimensions of the AgNW heating pattern are given in *SI Appendix*, Fig. S2*B*. Fig. 3*B* shows the heating performance of the AgNW/PI composite heater. With the increase of applied current, the maximum temperature increased. With 0.125 A current applied (5 V), the temperature of the heater rose from room temperature to 80 °C within 10 s. In the following experiments, the actuators and robots are operated in a constant room temperature environment (23 °C). The LCE ribbons yielded a large compressive strain (~30%) within the temperature window between 65 and 80 °C (*SI Appendix*, Fig. S3). The high heating efficiency of the AgNW/PI heater and the low responsive temperature of LCE together enabled the fast actuation of the thermal actuators. Of note is that most reported thermal bimorph actuators use two thermal-expanding materials with different CTEs while in this actuator one layer expands and the other layer shrinks. This opposite thermal response increases the bending amplitude and speed compared to traditional bimorph actuators. Our previous study of PDMS/LCE bimorph actuators provided a detailed analysis of the bending performance with respect to modulus ratio, thickness ratio, and heating temperature (8). A brief summary is provided in *SI Appendix*, section 3 and Fig. S4. Fig. 3*C* shows the folding angle of the side panel which is measured across the crease line as defined in the Kresling origami (*Inset* of Fig. 3*C*). With 0.125 A applied current, the effective folding angle reached 120° within 12 s. During the folding and unfolding, the resistance of the AgNW heater is fully recoverable, which enables the cyclic operation of the actuators (*SI Appendix*, Fig. S5). With a further increase of the current, the bending angle can go beyond 120°, which, however, could cause delamination between LCE and PI in the bimorph actuator. In the following discussion, we choose the current of 0.125 A for efficient and stable actuation.

Fig. 3 *D* and *E* show snapshots of the Kresling unit in the axial contraction mode, and in the bending mode (Movie S1), respectively. With the same current on both actuators, the lateral Kresling origami panels fold symmetrically along the predefined creases, causing a coupled rotation and contraction motion (no bending). Different currents on both actuators lead to a bending motion coupled with rotation and contraction. The contraction $(H_1 - h)/H_1$ and rotation angle α are defined by the relative distance and rotation of the top octagon panel with respect to the bottom panel. The bending angle θ is defined as the angle between the horizontal direction and the top octagon panel. Fig. 3*F* captures the contraction and rotation of the Kresling unit with the 0.125 A current on for 11 s and then turned off. A maximum height change of 25% and rotation angle of 22.4° were achieved. With the cooling of the heater and relaxation of the structure, the Kresling unit recovered within 10 s. Fig. 3*G* shows the minimum relative height (*Left*), the maximum rotation angle (*Middle*), and the maximum bending angle (*Right*) versus the applied current (or current difference). With 0.125 A on one actuator and 0 A on the counterpart, a maximum bending angle of 27.3° was achieved.

Bidirectional Locomotion of the Kresling Soft Robot. The crawling mechanism of caterpillars involves sequential activation and deactivation of multiple body segments as shown in Fig. 4*A*. The wave of cyclic crawling motion normally starts from the terminal segment and ends at the thoracic legs. A complete travel of contraction wave from tail to head is termed a "crawl." To demonstrate the feasibility of mimicking the crawling motion, we built a caterpillar-inspired crawling robot consisting of an interlaced series of three active Kresling units (each with two actuators marked in yellow) and four passive units (same setup but without actuators, marked in white). Fig. 4*B* shows schematically one cycle of crawling motion with sequential activation of Kresling units 1, 2, and 3 (Movie S2). When unit 1 is activated in the contraction mode, the friction force generated by the far-left passive unit is less than that by the rest of the robot. As a result, the tail of the robot slides rightward on the ground. In the next step, unit 1 is deactivated and cools down while unit 2 is activated at the same time. During this step, unit 1 extends to the original length while unit 2 contracts, resulting in a net force to translate the passive unit between units 1 and 2 to the right without moving the tail or the head of the soft robot. Because the heating and cooling of the heater require roughly the same duration of time

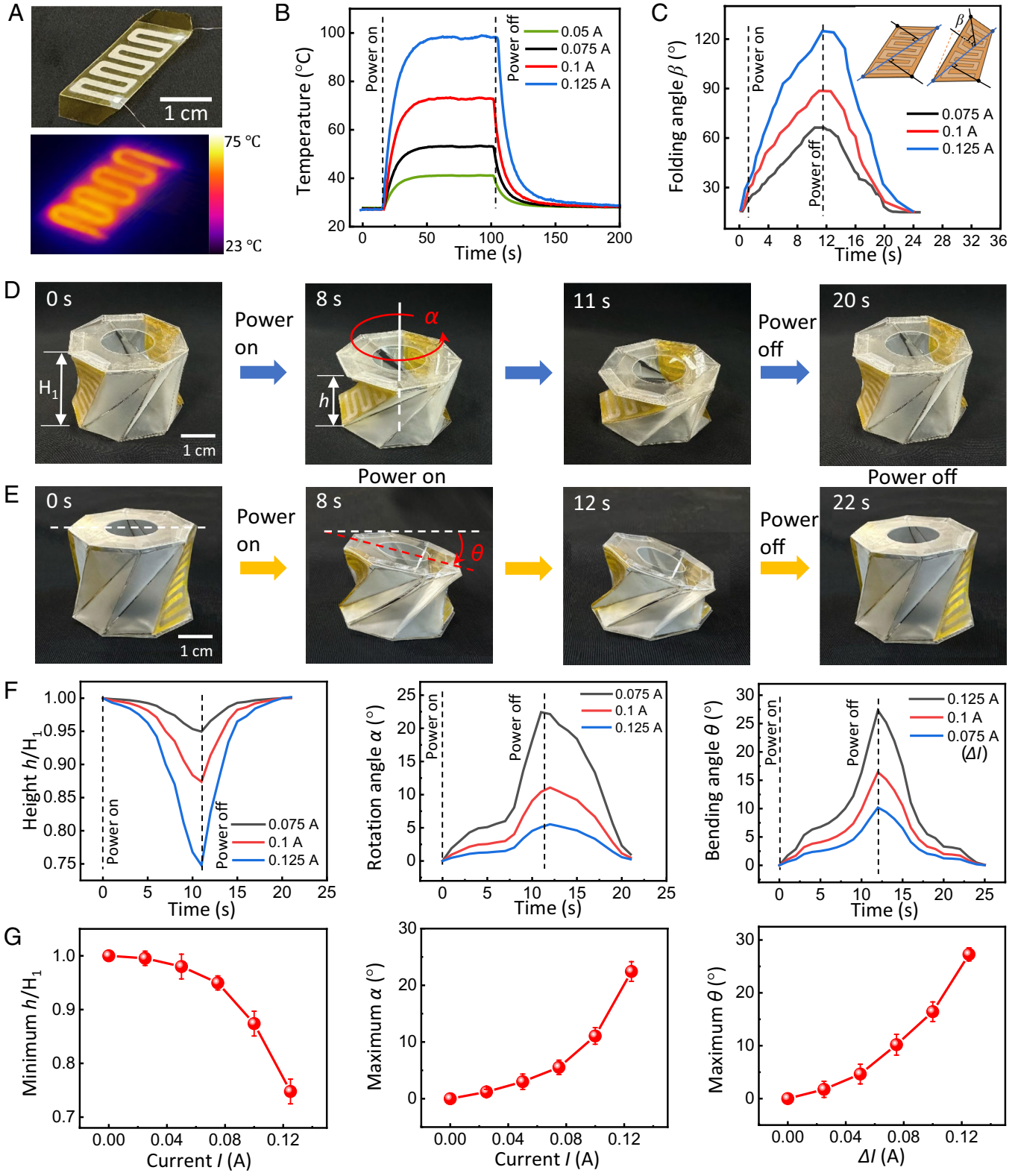

Fig. 3. Characterization of the thermal bimorph actuators and the Kresling unit. (*A*) Photograph and IR image of the thermal bimorph actuator. (*B*) The temperature changes of the AgNW/PI heaters with different currents on and off. (*C*) The folding angle (along the longest diagonal of the panel) of the thermal actuator with different currents on and off. The *Inset* schematic illustrates the folding angle. (*D*) Snapshots of the thermal actuators for contraction/extension of the origami robot segment. (*E*) Snapshots of the thermal actuators for bending of the origami robot segment. (*F*) Relative height change (*Left*), rotation angle (*Middle*), and bending angle (*Right*) versus time of the Kresling unit with different current inputs. (*G*) Minimum relative height (*Left*), maximum rotation angle (*Middle*), and maximum bending angle (*Right*) versus applied current (or current difference).

(~11 and 10 s), the deactivation of unit 1 and activation of unit 2 are programmed seamlessly. During the following step, unit 2 is deactivated, and unit 3 is activated, repeating the translation but for the next passive unit. In the final step, the deactivation of unit 3 pushes the far-right passive unit forward, completing a forward crawling cycle.

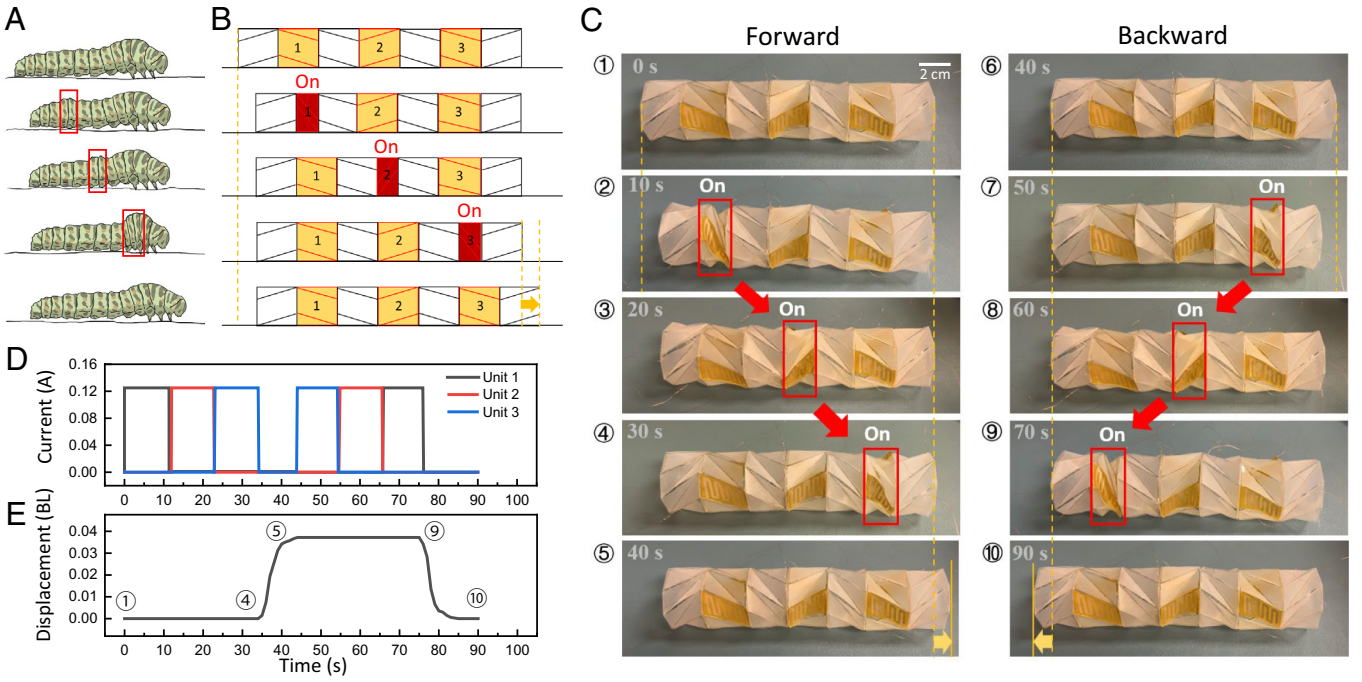

Fig. 4. Bidirectional locomotion of the Kresling soft robot. (*A*) Schematics of the caterpillars showing the motion. (*B*) Schematics of the soft robot with sequential activation and deactivation of three active units in between four passive units. (*C*) Snapshots of the soft robot in one cycle of forward motion followed by a cycle of backward locomotion. (*D*) Programmed current input of the three Kresling units to trigger bidirectional locomotion of the soft robot. (*E*) Rigid-body displacement (translation) of the soft robot finishing a cycle of forward crawling followed by a cycle of backward crawling.

During the crawling motion, friction is a key factor that affects the locomotion of our crawling robot. The condition for the locomotion is that the output force of the active units is larger than the friction force,

$$F_{output} \geq \mu W_{passive}, \quad [2]$$

where F_{output} is the output force of the active unit, $W_{passive}$ is the gravity force of one passive unit, and μ is the friction coefficient between PET and the substrate material. The output force of the Kresling unit has been measured and shown in *SI Appendix*, Fig. S6. For example, with applied current of 0.125 A, F_{output} = 0.23 N, $W_{passive} = 6.86 \times 10^{-3}$ N, the critical coefficient of friction for locomotion μ_c = 33.5. In the experiments, we have shown the locomotion of our soft robot (*SI Appendix*, Fig. S7*A*) on various surfaces, including synthetic leather mat, nylon cloth, and marble surface (*SI Appendix*, Fig. S7*B*). We measure the static friction coefficients of PET (major component of the robot body) on all three substrates using the setup in *SI Appendix*, Fig. S7*C*. The measured friction coefficients are shown in *SI Appendix*, Fig. S7*D*.

It is worth noting that the soft robot itself is a symmetric structure without any preference for crawling direction. The only factor that determines the crawling direction is the activation sequence of units 1, 2, and 3 (Fig. 4*C*, ①–⑤). With a reversed activation sequence (3, 2, and 1), as shown in Fig. 4*C*, ⑥–⑧, the soft robot can crawl backward to the original position. Fig. 4*D* shows the programmed current applied on the active units. Fig. 4*E* shows the rigid-body displacement (translation) of the soft robot finishing a cycle of forward crawling followed by a cycle of backward crawling. The cycles of forward and backward crawling each take ~40 s, which translates to an average crawling speed of 0.195 mm/s. The capability of bidirectional locomotion can be useful, for example, in search and rescue operations. In the 7-unit crawling robot, we adopted a symmetric design of chirality (*SI Appendix*, section 4). If we note the first passive unit as "L" in chirality and "R" for the opposite, the soft robot possesses the sequence LRRLRRL.

Steering Motion of the Kresling Soft Robot. In general, steering direction during locomotion has been challenging for soft robots. To navigate through complex tree branches and leaves, caterpillars have extremely flexible body segments between the thoracic legs and prolegs that can bend in any direction. Inspired by the caterpillar bending, we have demonstrated omnidirectional crawling with a programmable trajectory. The three active units of the robot are now delegated with different tasks—a "steering" unit (unit 2 in Fig. 5*A*) guiding the direction and two "driving" units (units 1 and 3 in Fig. 5*A*) for propulsion (locomotion). The schematics and photographs in Fig. 5 *A* and *B*, respectively, show the top–down snapshots of one cycle of the steering locomotion (Movie S3). The steering cycle starts by applying different currents on the two actuators in unit 2. The bending of unit 2 defines an initial curvature. Then, units 1 and 3 are activated sequentially both in the contraction mode. Like the peristaltic crawling locomotion, the tail is dragged forward in the third snapshot. With the deactivation of unit 1 and activation of unit 3, unit 2 and its two neighboring passive units travel forward following the curved direction. Finally, with the deactivation of unit 3, the head takes one step forward and turns away from its starting direction (Fig. 5*B*). With the local bending capability, the soft robot can be programmed to follow any in-plane trajectory while respecting a maximum curvature limit. For example, the robot can be programmed to follow an S-shaped trajectory (Fig. 5*C* and Movie S4) or even a tree crotch (Fig. 5*D*). The key to programming the S-shaped trajectory is to actively control and follow the real-time curvature of the locomotion. Fig. 5*E* shows the difference of input current ΔI on the two actuators of the steering unit 2 with respect to time. From 0 to 400 s, the snapshots ①, ②, and ③ show a gradual increase of the bending curvature (from ρ_1 = 25.8 cm to ρ_2 = 15.5 cm) due to the increasing ΔI (from 0.075 A to 0.125 A). Then, the steering

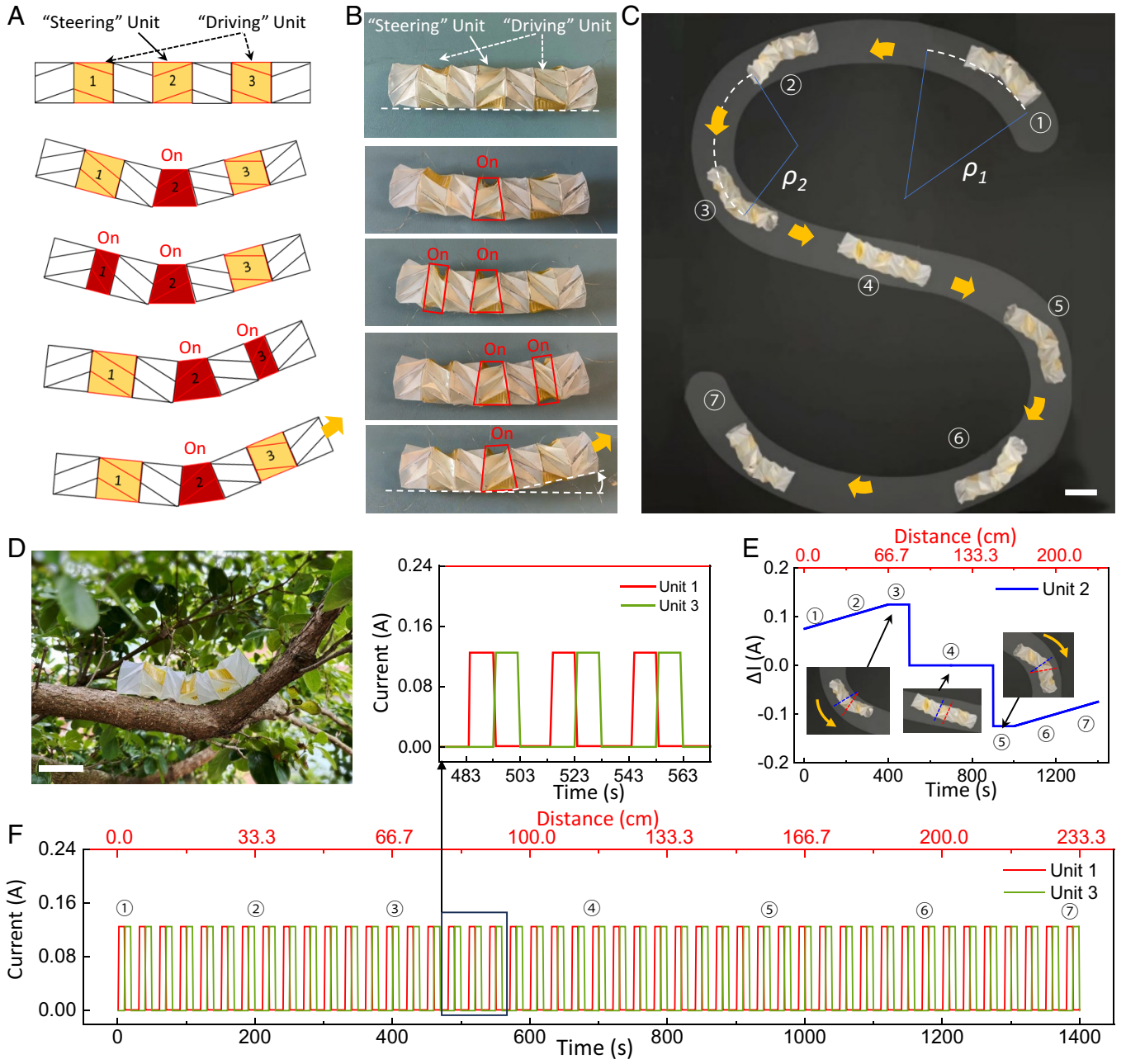

Fig. 5. Steering locomotion of the Kresling soft robot. (*A* and *B*) Schematics and corresponding photographs of the soft bot showing sequential heating and cooling for steering motion. It consists of three active units, i.e., one for steering and two for driving, as well as four passive units which amplify and facilitate the steering motion. (*C*) Programmed locomotion of the soft robot following an S-shaped trajectory. (Scale bar, 5 cm.) (*D*) Photograph of the soft robot moving along a curved tree branch. (Scale bars, 5 cm.) (*E*) Programmed current input on the two actuators of Kresling unit 2 for the S-shaped locomotion. (*F*) Cyclic current input on the two driving units 1 and 3 for the S-shaped locomotion. (with a zoomed-in view of three actuation cycles)

unit is deactivated for 400 s to complete a period of rectilinear motion (snapshot ④). From 900 to 1,200 s, a negative ΔI with decreasing magnitude (from −0.125 to −0.075 A) is applied to the steering unit 2 for reversed bending. Due to the symmetric Kresling structure with two addressable bimorph actuators, the second half of the trajectory (from ⑤ to ⑦) resembles the first half with the negative curvature, which completes an S-shape. Fig. 5*F* shows the cyclic current input on the two driving units 1 and 3 for the S-shaped locomotion.

Robotic Module Design of the Kresling Origami Units. Modular robots are constructed from multiple interchangeable and customizable modules, each of which contributes to their overall functionality (52, 53). Incorporating the modular concept into soft robots, we achieve versatility, customizability, scalability, and even better adaptability to the environment (54). The Kresling origami units are excellent modular components due to their multiple deformation modes and symmetric design.

We propose a two-level module design for Kresling robots: single-unit modules and multi-unit modules (Fig. 6*A*). The single-unit modules can be divided into two types, the active units which are equipped with actuators, and the passive units without actuators. With active units and passive units connected through the *Top/Bottom* octagon panels, a multi-unit module can be constructed with properly designated functions. To name the modules, 1 active unit and 1 passive unit would form an AP module; and similarly, 1 passive unit, 1 active unit, and 1 passive unit in sequence would form a PAP module.

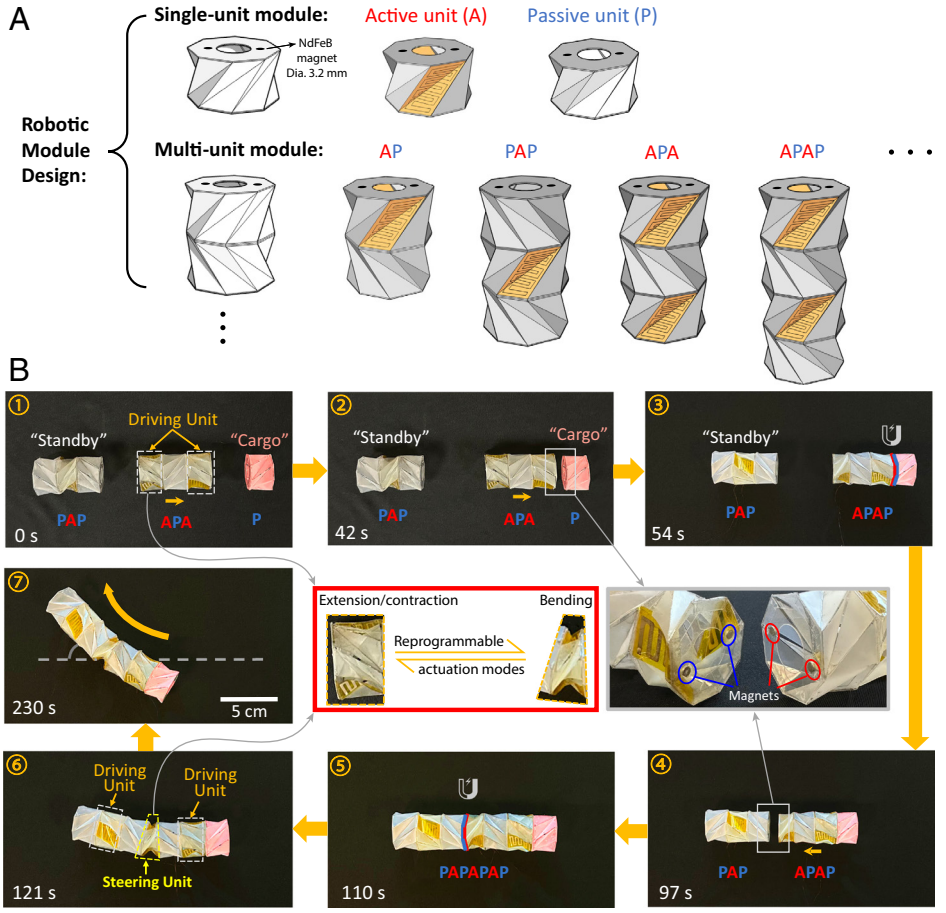

Fig. 6. Robotic module design with reprogrammable actuation. (*A*) Schematics of the robotic module design showing examples of single-unit modules and multiple-unit modules. Note that AP represents a module with 1 active unit and 1 passive unit. (*B*) Demonstration of an APA module picking up a cargo P module, assembling with a separate PAP module, and enabling steering functionality. The central *Inset* figure, highlighted with a red contour, indicates that for one of the driving units in ①, its actuation mode is reprogrammed to serve as the steering unit in ⑥ with all modules connected (i.e., PAPAPAP). The other *Inset* figure, highlighted with a grey contour, illustrates the modular magnetic interconnection during the navigation process.

We demonstrate the module concept by having an APA module pick up a cargo P module and then assemble with a PAP module for obtaining steering functionality (Fig. 6*B* and Movie S5). To start, a PAP module sits on the table in "standby" mode. Note that this module has a symmetrical configuration with only one active unit in the center. The PAP module can be activated, but unable to locomote, unless an asymmetric "feet" design is introduced (55). An APA module, on the other hand, has two active units which can be activated sequentially to navigate either forward or backward. In the first stage, both active units of the APA module serve as driving units to navigate rightward to approach the cargo P module (a single passive unit). When the two modules are close enough, the opposing octagon panels with embedded magnets attract each other and assemble into one (*Inset* of Fig. 6*B*). The new APAP module now carries the cargo P module on the tail. By changing the actuation sequence of the two active units, the APAP module can switch locomotion direction and move left. Again, when the APAP module approaches the PAP module, they merge through the embedded magnets and become a combined PAPAPAP module. Compared with the APA module, the PAPAPAP module is capable of not only forward and backward locomotion but also steering motion. Movie S5 captures this transition from linear locomotion to steering locomotion (the two phases of Movie S5 were taken separately and joined together as one). Of note is that the middle active unit, which initially serves as a driving unit, now reprograms its role to guide the steering curvature of the combined PAPAPAP module for bending deformation. With the steering function, the crawling robot can carry the cargo deviating from its original 1-D space. This modular design concept can be extended by increasing the number of units and sequence of the active and passive units, and possibly 3D assembly with customized connectors.

Discussion

Inspired by the locomotion of the caterpillar, we have designed, fabricated, and characterized a multimodal Kresling origami unit with two soft electrothermal actuators directly integrated with the Kresling structure. The LCE and PI components form a bimorph thermal actuator structure that sandwiches a deformable heater made of a serpentine-shaped AgNW network, enabling sharp, reversible bending along the crease line of the Kresling structure. We characterized the two deformation modes of the Kresling unit, contraction mode and bending mode, by heating the two actuators in a programmable manner. A maximum height change of 25% and rotation angle of 22.4° were obtained within 12 s of Joule heating (6.25 V) in the contraction mode. In the bending mode, a maximum bending angle of 27.3° was achieved with 0.125 A on one actuator and 0 A on the other actuator.

To demonstrate a soft robot that mimics the multi-degree-of-freedom motions (e.g., crawling and steering) of caterpillars, we assemble a total of seven Kresling units, consisting of three active units and four passive units, and arrange them with

alternating chirality. Bidirectional locomotion is achieved by programming actuation sequences. Each cycle of crawling takes ~40 s, which translates to an average crawling speed of 0.195 mm/s. In addition, the steering motion of the soft robot is achieved with real-time local bending angle control. The soft robot is programmed to follow an S-shaped trajectory with a constantly changing radius of curvature. Compared with reported soft locomotive robots (1, 8–11, 13, 14, 56–60) (*SI Appendix*, Table S1), the combination of bidirectional and steering locomotion largely enhances the mobility of the soft robot. However, compared with other reported crawling/inching robots, our crawling robot possesses relatively low locomotion speed. The speed can potentially be improved by increasing the thermal conductivity of the LCE layer, decreasing the thickness of the bimorph actuators, or introducing mechanical instability in the design of the unit cells.

Finally, we propose a two-level robotic module design of the Kresling origami robot. By mimicking the rich kinematics of the caterpillar segments, each of our robot modular features reprogrammable actuation modes, i.e., extension/contraction and bending. The desired deformation modes of the modular units, bidirectional and/or steering, can be achieved on the fly. We demonstrate the modular design of the origami robot with an active robotic module picking up cargo and assembling with another robotic module to enable steering functions. The modular concept, empowered by the bioinspired multi-degree-of-freedom soft origami structure, holds promising potential for a new generation of soft robots that can morph, repair, and enhance functionality.

Materials and Methods

LCE Ribbon Fabrication. The LCE ribbons were fabricated following the thiol-acrylate Michael addition reaction method (61). First, 2 g of the liquid crystal mesogenic monomer, 1,4-bis-[4-(3-acryloyloxypropyloxy)benzoyloxy]-2-methylbenzene (RM 257) was dissolved in 0.7 g of toluene at 85 °C and cooled down to room temperature. Then, 0.42 g of the chain extender 2,2′-(ethylenedioxy) diethanethiol (EDDET, Sigma-Aldrich), 0.18 g of cross-linker pentaerythritol tetrakis (3-mercapto propionate) (PETMP, Sigma-Aldrich), and 0.012 g of the photoinitiator (2-hydroxyethoxy)-2-methylpropiophenone (HHMP, Sigma-Aldrich) were mixed and dissolved at 85 °C. Finally, 0.288 g of catalyst (dipropyl amine, Sigma-Aldrich) solution (2 wt%, in toluene) was added to the solution. After fully mixed and degassed, the solution was poured in a mold and cured for 24 h. The dried LCE sample was uniaxially stretched to 100% strain. The stretched sample was exposed to ultraviolet (UV) light (365 nm) at an intensity of 20 mJ/cm^2 for 10 min.

Synthesis of AgNWs. First, 60 mL of a 0.147 M polyvinylpyrrolidone (PVP) (MW ~ 40,000, Sigma-Aldrich) solution in ethylene glycol (EG) was added to a flask, to which a stir bar was added; the solution was then suspended in an oil bath (temperature 151.5 °C) and heated for 1 h under magnetic stirring (150 rpm). Then, 200 μL of a 24 M $CuCl_2$ ($CuCl_2 \cdot 2H_2O$, 99.999+%, Sigma-Aldrich) solution in EG was injected into the PVP solution. The mixture solution was then injected with 60 mL of a 0.094 M $AgNO_3$ (99+%, Sigma-Aldrich) solution in EG (62).

Fabrication of the Thermal Actuation Enabled the Kresling Unit. The AgNW solution was drop-cast on a sacrificial glass slide, which was then placed onto a hot plate at 50 °C to evaporate the solvent. After the solvent was evaporated, PI resin (NeXolve) was drop-cast and spin-coated on top of the AgNW network. After curing at 140 °C for an hour, the AgNW/PI composite film (10 μm thick) was then laser cut into designed serpentine patterns. After laser cutting, the AgNW/PI heater was transferred to the commercial PI tape (60 μm thick, Kapton) on the side with adhesive. Then, the heater/PI tape composite and synthesized LCE film (300 μm thick) were put in the plasma chamber (Plasma Cleaner PDC-32G, HARRICK PLASMA) for 30 s. After the plasma treatment, the treated heater/PI tape and LCE were laminated together with 50 kPa pressure for 2 min. The Cu wires were attached to the two ends of the conductive patterns by silver epoxy (MG Chemicals). The fabrication of the LCE/AgNW/PI bimorph actuator was finalized by trimming it into the parallelogram shape from the octagon Kresling origami design. Of note is that the mesogen alignment of the LCE layer is perpendicular to the longer diagonal line of the parallelogram, i.e., the folding crease. The remaining part of the Kresling unit was folded and assembled with a piece of laser-cut PET sheet (50 μm thick). The two parallelogram side panels, in opposing directions, were replaced by two LCE/AgNW/PI actuators.

Numerical Simulation of Kresling Origami Units. We used a reduced-order model to simulate the multi-degree-of-freedom of the robot segment involving contraction, twist, and bending. Our analysis was based on the nonlinear bar-and-hinge method (63, 64). As shown in *SI Appendix*, Fig. S8, we utilized bar elements along mountain and valley creases to model axial deformation, and rotational springs along actuators to capture folding. We described the kinematics by the total Lagrangian approach, taking reference to the initial configurations. Additionally, we used the standard linear elasticity as the constitutive relationship. The nonlinear equilibrium equation is formulated as follows:

$$\boldsymbol{R}(\boldsymbol{u}) = \boldsymbol{T}(\boldsymbol{u}) - \boldsymbol{F}(\boldsymbol{u}) = \boldsymbol{T}(\boldsymbol{u}) - \chi(\boldsymbol{u})\boldsymbol{f} = \boldsymbol{0}. \quad [3]$$

Here, $\boldsymbol{R}$ denotes the residual force vector, $\boldsymbol{u}$ refers to the displacement vector, the vector $\boldsymbol{F}$ contains the forces applied to the nodes of the bar-and-hinge system, $\boldsymbol{T}$ denotes internal force vector, χ is known as the load factor that controls the magnitude of the external loads, and $\boldsymbol{f}$ is a unit reference load vector. We adopted an incremental-iterative procedure to solve Eq. **3**. The nonlinear solution scheme is detailed in *SI Appendix*, section 2, and the algorithm containing the pseudocode of the scheme is provided in *SI Appendix*, Table S3. Our implementation was performed using an in-house MATLAB code inspired by the open-source software MERLIN.

Data, Materials, and Software Availability. All data are included in the article and/or supporting information.

ACKNOWLEDGMENTS. We would like to thank S.-Y. Lee for her help with the LCE fabrication. The authors at Princeton University acknowledge partial support from the Margareta E. Augustine Professorship of Engineering and the National Science Foundation (NSF) (CMMI-2323276). The authors at North Carolina State University acknowledge the financial support from the NSF (TI-2122841 and CMMI- 2134664) and NIH (1R01HD108473). This publication was supported by the Princeton University Library Open Access Fund.

Author affiliations: [a]Department of Mechanical and Aerospace Engineering, North Carolina State University, Raleigh, NC 27695; [b]Department of Civil and Environmental Engineering, Princeton University, Princeton, NJ 08544; and [c]Princeton Materials Institute, Princeton University, Princeton, NJ 08544

1. R. F. Shepherd *et al.*, Multigait soft robot. *Proc. Natl. Acad. Sci. U.S.A.* **108**, 20400–20403 (2011).
2. D. Rus, M. T. Tolley, Design, fabrication and control of soft robots. *Nature* **521**, 467–475 (2015).
3. C. Laschi, B. Mazzolai, M. Cianchetti, Soft robotics: Technologies and systems pushing the boundaries of robot abilities. *Sci. Robot.* **1**, eaah3690 (2016).
4. H. Zhao, K. O'brien, S. Li, R. F. Shepherd, Optoelectronically innervated soft prosthetic hand via stretchable optical waveguides. *Sci. Robot.* **1**, eaai7529 (2016).
5. A. L. Evenchik, A. Q. Kane, E. Oh, R. L. Truby, Electrically controllable materials for soft, bioinspired machines. *Annu. Rev. Mater. Res.* **53**, 225–251 (2023).
6. C. Lee *et al.*, Soft robot review. *Int. J. Control. Autom.* **15**, 3–15 (2017).
7. N. El-Atab *et al.*, Soft actuators for soft robotic applications: A review. *Adv. Intell. Syst.* **2**, 2000128 (2020).
8. S. Wu, Y. Hong, Y. Zhao, J. Yin, Y. Zhu, Caterpillar-inspired soft crawling robot with distributed programmable thermal actuation. *Sci. Adv.* **9**, eadf8014 (2023).
9. S. Wu *et al.*, Symmetry-breaking actuation mechanism for soft robotics and active metamaterials. *ACS Appl. Mater. Interfaces* **11**, 41649–41658 (2019).
10. Y. Xiao *et al.*, Anisotropic electroactive elastomer for highly maneuverable soft robotics. *Nanoscale* **12**, 7514–7521 (2020).
11. M. Rogóż, H. Zeng, C. Xuan, D. S. Wiersma, P. Wasylczyk, Light-driven soft robot mimics caterpillar locomotion in natural scale. *Adv. Opt. Mater.* **4**, 1689–1694 (2016).
12. L. Van Griethuijsen, B. Trimmer, Locomotion in caterpillars. *Biol. Rev.* **89**, 656–670 (2014).
13. Q. Ze *et al.*, Soft robotic origami crawler. *Sci. Adv.* **8**, eabm7834 (2022).
14. T. Xu, J. Zhang, M. Salehizadeh, O. Onaizah, E. Diller, Millimeter-scale flexible robots with programmable three-dimensional magnetization and motions. *Sci. Robot.* **4**, eaav4494 (2019).
15. L. F. Muff *et al.*, Modular design of a polymer-bilayer-based mechanically compliant worm-like robot. *Adv. Mater.* **35**, e2210409 (2023).
16. T. C. Hull, *Origametry: Mathematical Methods in Paper Folding* (Cambridge University Press, 2020).

17. S.-J. Kim, D.-Y. Lee, G.-P. Jung, K.-J. Cho, An origami-inspired, self-locking robotic arm that can be folded flat. *Sci. Robot.* **3**, eaar2915 (2018).
18. B. Kresling, "Natural twist buckling in shells: from the hawkmoth's bellows to the deployable Kresling-pattern and cylindrical miura-ori" in *Proceedings of the 6th International Conference on Computation of Shell and Spatial Structures IASS-IACM 2008: "Spanning Nano to Mega,"*J. F. Abel, J. R. Cooke, Eds. (Cornell University, Ithaca, NY, 2008), pp. 18–21.
19. S. Wu *et al.*, Stretchable origami robotic arm with omnidirectional bending and twisting. *Proc. Natl. Acad. Sci. U.S.A.* **118**, e2110023118 (2021).
20. D. Melancon, A. E. Forte, L. M. Kamp, B. Gorissen, K. Bertoldi, Inflatable origami: Multimodal deformation via multistability. *Adv. Funct. Mater.* **32**, 2201891 (2022).
21. C. Zhang *et al.*, Plug & play origami modules with all-purpose deformation modes. *Nat. Commun.* **14**, 4329 (2023).
22. M. T. Tolley *et al.*, A resilient, untethered soft robot. *Soft Rob.* **1**, 213–223 (2014).
23. Y. Tang *et al.*, Leveraging elastic instabilities for amplified performance: Spine-inspired high-speed and high-force soft robots. *Sci. Adv.* **6**, eaaz6912 (2020).
24. S. Yao, J. Cui, Z. Cui, Y. Zhu, Soft electrothermal actuators using silver nanowire heaters. *Nanoscale* **9**, 3797–3805 (2017).
25. Q. He *et al.*, Electrically controlled liquid crystal elastomer–based soft tubular actuator with multimodal actuation. *Sci. Adv.* **5**, eaax5746 (2019).
26. Y. Zhao *et al.*, Twisting for soft intelligent autonomous robot in unstructured environments. *Proc. Natl. Acad. Sci. U.S.A.* **119**, e2200265119 (2022).
27. Y. Li *et al.*, Three-dimensional thermochromic liquid crystal elastomer structures with reversible shape-morphing and color-changing capabilities for soft robotics. *Soft Matter* **18**, 6857–6867 (2022).
28. S. Wu, G. L. Baker, J. Yin, Y. Zhu, Fast thermal actuators for soft robotics. *Soft Rob.* **9**, 1031–1039 (2022).
29. E. Acome *et al.*, Hydraulically amplified self-healing electrostatic actuators with muscle-like performance. *Science* **359**, 61–65 (2018).
30. T. Li *et al.*, Fast-moving soft electronic fish. *Sci. Adv.* **3**, e1602045 (2017).
31. J. Shintake, V. Cacucciolo, D. Floreano, H. Shea, Soft robotic grippers. *Adv. Mater.* **30**, 1707035 (2018).
32. W. Hu, G. Z. Lum, M. Mastrangeli, M. Sitti, Small-scale soft-bodied robot with multimodal locomotion. *Nature* **554**, 81–85 (2018).
33. G. Mao *et al.*, Soft electromagnetic actuators. *Sci. Adv.* **6**, eabc0251 (2020).
34. Y. Kim, H. Yuk, R. Zhao, S. A. Chester, X. Zhao, Printing ferromagnetic domains for untethered fast-transforming soft materials. *Nature* **558**, 274–279 (2018).
35. J. C. Nawroth *et al.*, A tissue-engineered jellyfish with biomimetic propulsion. *Nat. Biotechnol.* **30**, 792–797 (2012).
36. I. Must, E. Sinibaldi, B. Mazzolai, A variable-stiffness tendril-like soft robot based on reversible osmotic actuation. *Nat. Commun.* **10**, 1–8 (2019).
37. L. Chen *et al.*, High-performance, low-voltage, and easy-operable bending actuator based on aligned carbon nanotube/polymer composites. *ACS Nano* **5**, 1588–1593 (2011).
38. H. Kim *et al.*, Biomimetic color changing anisotropic soft actuators with integrated metal nanowire percolation network transparent heaters for soft robotics. *Adv. Funct. Mater.* **28**, 1801847 (2018).
39. E. Hawkes *et al.*, Programmable matter by folding. *Proc. Natl. Acad. Sci. U.S.A.* **107**, 12441–12445 (2010).
40. S. Yao, J. Yang, F. R. Poblete, X. Hu, Y. Zhu, Multifunctional electronic textiles using silver nanowire composites. *ACS Appl. Mater. Interfaces* **11**, 31028–31037 (2019).
41. J. W. Lee *et al.*, Soft, thin skin–mounted power management systems and their use in wireless thermography. *Proc. Natl. Acad. Sci. U.S.A.* **113**, 6131–6136 (2016).
42. C. Wang *et al.*, Soft ultrathin electronics innervated adaptive fully soft robots. *Adv. Mater.* **30**, 1706695 (2018).
43. N. Nayakanti, S. H. Tawfick, A. J. Hart, Twist-coupled kirigami cells and mechanisms. *Extreme Mech. Lett.* **21**, 17–24 (2018).
44. S. Hong *et al.*, Highly stretchable and transparent metal nanowire heater for wearable electronics applications. *Adv. Mater.* **27**, 4744–4751 (2015).
45. S. Choi *et al.*, Stretchable heater using ligand-exchanged silver nanowire nanocomposite for wearable articular thermotherapy. *ACS Nano* **9**, 6626–6633 (2015).
46. F. Xu, Y. Zhu, Highly conductive and stretchable silver nanowire conductors. *Adv. Mater.* **24**, 5117–5122 (2012).
47. W. Zhou *et al.*, Gas-permeable, ultrathin, stretchable epidermal electronics with porous electrodes. *ACS Nano* **14**, 5798–5805 (2020).
48. Z. Cui, F. R. Poblete, Y. Zhu, Tailoring the temperature coefficient of resistance of silver nanowire nanocomposites and their application as stretchable temperature sensors. *ACS Appl. Mater. Interfaces* **11**, 17836–17842 (2019).
49. S. Wu *et al.*, A biaxially stretchable and self-sensing textile heater using silver nanowire composite. *ACS Appl. Mater. Interfaces* **13**, 59085–59091 (2021).
50. C. Yakacki *et al.*, Tailorable and programmable liquid-crystalline elastomers using a two-stage thiol–acrylate reaction. *RSC Adv.* **5**, 18997–19001 (2015).
51. M. O. Saed, A. H. Torbati, D. P. Nair, C. M. Yakacki, Synthesis of programmable main-chain liquid-crystalline elastomers using a two-stage thiol–acrylate reaction. *JoVE* **107**, e53546 (2016).
52. P. Moubarak, P. Ben-Tzvi, Modular and reconfigurable mobile robotics. *Rob. Autonom. Syst.* **60**, 1648–1663 (2012).
53. C. H. Belke, J. Paik, Mori: A modular origami robot. *IEEE/ASME Trans. Mech.* **22**, 2153–2164 (2017).
54. C. Zhang, P. Zhu, Y. Lin, Z. Jiao, J. Zou, Modular soft robotics: Modular units, connection mechanisms, and applications. *Adv. Intell. Syst.* **2**, 1900166 (2020).
55. A. Pantula *et al.*, Untethered unidirectionally crawling gels driven by asymmetry in contact forces. *Sci. Robot.* **7**, eadd2903 (2022).
56. A. Rafsanjani, Y. Zhang, B. Liu, S. M. Rubinstein, K. Bertoldi, Kirigami skins make a simple soft actuator crawl. *Sci. Robot.* **3**, eaar7555 (2018).
57. Y. He *et al.*, A highly sensitive, reversible, and bidirectional humidity actuator by calcium carbonate ionic oligomers incorporated poly (vinylidene fluoride). *Adv. Funct. Mater.* **31**, 2101291 (2021).
58. B. Shin *et al.*, Hygrobot: A self-locomotive ratcheted actuator powered by environmental humidity. *Sci. Robot.* **3**, eaar2629 (2018).
59. M. Duduta, D. R. Clarke, R. J. Wood, "A high speed soft robot based on dielectric elastomer actuators" in *2017 IEEE International Conference on Robotics and Automation (ICRA)*, A. Okamura, Ed. (IEEE, Singapore, 2017), pp. 4346–4351.
60. F. Ge, R. Yang, X. Tong, F. Camerel, Y. Zhao, A multifunctional dye-doped liquid crystal polymer actuator: Light-guided transportation, turning in locomotion, and autonomous motion. *Angew. Chem.* **130**, 11932–11937 (2018).
61. M. Barnes, R. Verduzco, Direct shape programming of liquid crystal elastomers. *Soft Matter* **15**, 870–879 (2019).
62. Y. Sun, B. Gates, B. Mayers, Y. Xia, Crystalline silver nanowires by soft solution processing. *Nano Lett.* **2**, 165–168 (2002).
63. S. Zang, D. Misseroni, T. Zhao, G. H. Paulino, Kresling origami mechanics explained: Experiments and theory. *J. Mech. Phys. Solids*, https://doi.org/10.1016/j.jmps.2024.105630 (2024).
64. K. Liu, G. H. Paulino, Nonlinear mechanics of non-rigid origami: An efficient computational approach. *Proc. R. Soc. A: Math., Phys. Eng. Sci.* **473**, 20170348 (2017).